Facile Pathways to Synthesize Perovskite Strontium Cobalt Oxides

Sicheng Lu, Fang Yin, Yujia Wang, Nianpeng Lu, Lei Gao, Huining Peng, Yingjie Lyu, Youwen Long, Jia Li,* and Pu Yu*

Topotactic phase transition obtains extensive research attention due to its associated rich physics as well as a promising potential application. Particularly, the oxygen incorporation into brownmillerite oxides leads to the structural transition into perovskite oxides with distinct magnetic and electronic properties. Using brownmillerite $SrCoO_{2.5}$ (BM-SCO), two novel pathways are revealed to achieve the topotactic phase transition into its corresponding perovskite $SrCoO_3$ (P-SCO). It is demonstrated that by using aqueous alkali as the electrolyte during gating, the negative biased voltage triggers a rapid transition into P-SCO, which is attributed to the presence of strong oxidizing hydroxyl radicals. While surprisingly, it is observed that the acid solution with rich protons can also trigger an unexpected phase transition from BM-SCO into P-SCO in a much faster manner. With density functional theory calculations, this transition is elucidated as a proton-assist ionic disproportionation, in which the Co ions are simultaneously oxidized and reduced, while the latter one is dissolved within the solution. These case studies not only achieve a deep understanding of the structural phase transition in BM-SCO but also shed new light on the topotactic phase transition of complex oxides.

1. Introduction

Over the last few decades, transition metal oxides (TMOs) have been demonstrating great potential for novel functional devices due to their rich properties, such as superconductivity, colossal magnetoresistance, multiferroic, electrocatalysis, and solid oxide fuel cells.[1–5] Multivalence TMOs have attracted extensive research attention for their electronic and magnetic properties, largely originating from their flexible (tunable) valence state of TM ions. Recently, the topotactic phase transition through oxygen evolution obtained a revival of research interest in manipulating the valence state of TM ions with TMOs through the manipulation of the oxygen content, which demonstrates promising potential application in energy conversion, smart window, and particularly neuromorphic computation devices.[6–9]

Strontium cobalt oxides are a model system of multivalence TMOs, in which a pronounced topotactic phase transition between brownmillerite $SrCoO_{2.5}$ (BM-SCO)[10] and perovskite $SrCoO_{3-\delta}$ (P-SCO),[11] drives a phase switching between insulating antiferromagnetic state and metallic ferromagnetic state, demonstrating an exotic magnetoelectric coupling,[12,13] and resistive switch.[14,15] During the studies, it was found that the synthesis of high-valence P-SCO is of fundamental challenge, because of the higher Gibbs free energy[16] and reduced oxygen vacancy formation energy of high-valence Co^{4+}, especially for epitaxially strained thin films.[17,18] Many efforts have been devoted to synthesizing P-SCO from BM-SCO,[19–30] which could be classified into two categories, high-temperature annealing under an oxidative atmosphere and electrochemical redox reaction within an electrolyte. Over the course of studies, oxidizing agent (e.g., oxygen, ozone, hydrogen peroxide, etc.[31–34]) emerges as essential parameter to trigger the phase transition. An interesting and immediate question emerges as to whether the hydroxyl radical, a more powerful oxidizer than hydrogen peroxide, can trigger a more efficient phase transition than others. This question becomes particularly important considering the fact that it remains largely unresolved for the mechanism of the ionic-liquid-gating (ILG) induced oxidization. Furthermore, a recent study[35] reveals that BM-SCO is dissolvable within weak acids and thus can serve as a promising sacrificial layer for the

S. Lu, Y. Wang, H. Peng, Y. Lyu, P. Yu
State Key Laboratory of Low Dimensional Quantum Physics
and Department of Physics
Tsinghua University
Beijing 100084, China
E-mail: yupu@mail.tsinghua.edu.cn
S. Lu, Y. Wang, H. Peng, Y. Lyu, P. Yu
Frontier Science Center for Quantum Information
Beijing 100084, China
F. Yin, J. Li
Institute of Materials Research
Tsinghua Shenzhen International Graduate School
Tsinghua University
Shenzhen 518055, China
E-mail: li.jia@sz.tsinghua.edu.cn
N. Lu, L. Gao, Y. Long
Beijing National Laboratory for Condensed Matter Physics
Institute of Physics
Chinese Academy of Sciences
Beijing 100190, China
N. Lu, Y. Long
Songshan Lake Materials Laboratory
Dongguan, Guangdong 523808, China
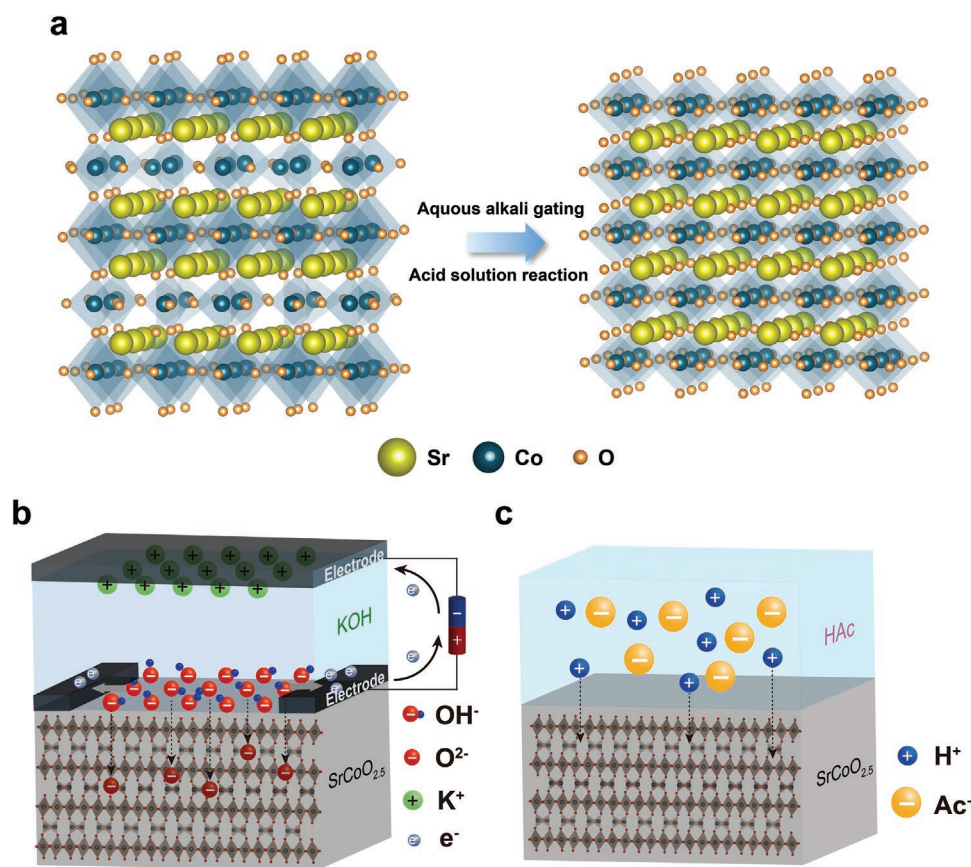
Figure 1. a) Illustrations of structural phase transition from Brownmillerite $SrCoO_{2.5}$ (BM-SCO) to perovskite $SrCoO_3$ (P-SCO) through different methods. b) Schematic illustration of electric-field-induced oxidation of BM-SCO through aqueous alkali gating (AAG). c) Phase transitions from BM-SCO to P-SCO through acid solution reaction (ASR).

fabrication of high-quality freestanding oxide thin films. Nevertheless, the structural transition of the BM-SCO within acid with proton remains unexplored.

In this work, we demonstrated two novel pathways to trigger the oxygen ionic evolution within BM-SCO, leading to the phase transition into P-SCO (**Figure 1**a). We revealed that the aqueous alkali gating (AAG) could trigger a rapid phase transition due to the presence of strong oxidizing hydroxyl radicals (Figure 1b). While surprisingly, the acid solution can also lead to a distinct structural transition into P-SCO phase, which was termed as acid solution reaction (ASR) method in this study (Figure 1c). These two newly developed methods show unprecedented reaction and phase transition rates than previous methods, which therefore enrich the pathways to manipulate the oxygen ionic evolution for TMOs.

In this study, we first prepared high-quality BM-SCO thin films with a thickness of ≈30 nm through pulsed laser deposition on (001)-oriented $(LaAlO_3)_{0.3}$-$(SrAl_{0.5}Ta_{0.5}O_3)_{0.7}$ (LSAT, a = 3.868 Å) substrates (see Experimental Section). The as-prepared samples show an excellent crystalline quality with the atomic stacking of oxygen tetrahedra and octahedra along the film normal, as evidenced by the superlattice peaks of the X-ray diffraction (XRD) results. With these films, we then explored various strategies to achieve the phase transition from BM-SCO to P-SCO.

2. Results

First, to verify the influence of the hydroxyl radical during the phase transition, we carried out similar gating measurements as the previous ILG study[12] while using the 0.1 м KOH solution as the liquid electrolyte. The in situ voltage dependence XRD studies reveal that the topotactic phase transition occurs at a critical voltage of −0.6 V, which is clearly lower than the value (i.e., −1.0 V) required for the ILG method[12] (**Figure 2**a). Furthermore, the phase transition time is ≈ 2 min with a gating voltage of −1 V, which is much faster than the previously employed ILG method even with a larger gating voltage.[12]

Surprisingly, we found that by simply soaking the BM-SCO thin film into an acid solution (36% acetic acid (HAc)) at room temperature for an extremely short time of 2 s, a distinct structural transition can be triggered, as shown in Figure 2c. This XRD result is very close to that obtained with the ILG and AAG methods. To ascertain this structural transition, we performed detailed long-range XRD scans for samples obtained from both AAG and ASR methods. To provide a suitable reference, we also measured the P-SCO sample obtained through the *ex-situ* ozone annealing (EOA) method, in which the BM-SCO was annealed in an ozone atmosphere at 300 °C for 40 min.[31] In the XRD results shown in Figure 2d, the as-grown BM-SCO thin film shows a series of characteristic superlattice peaks,
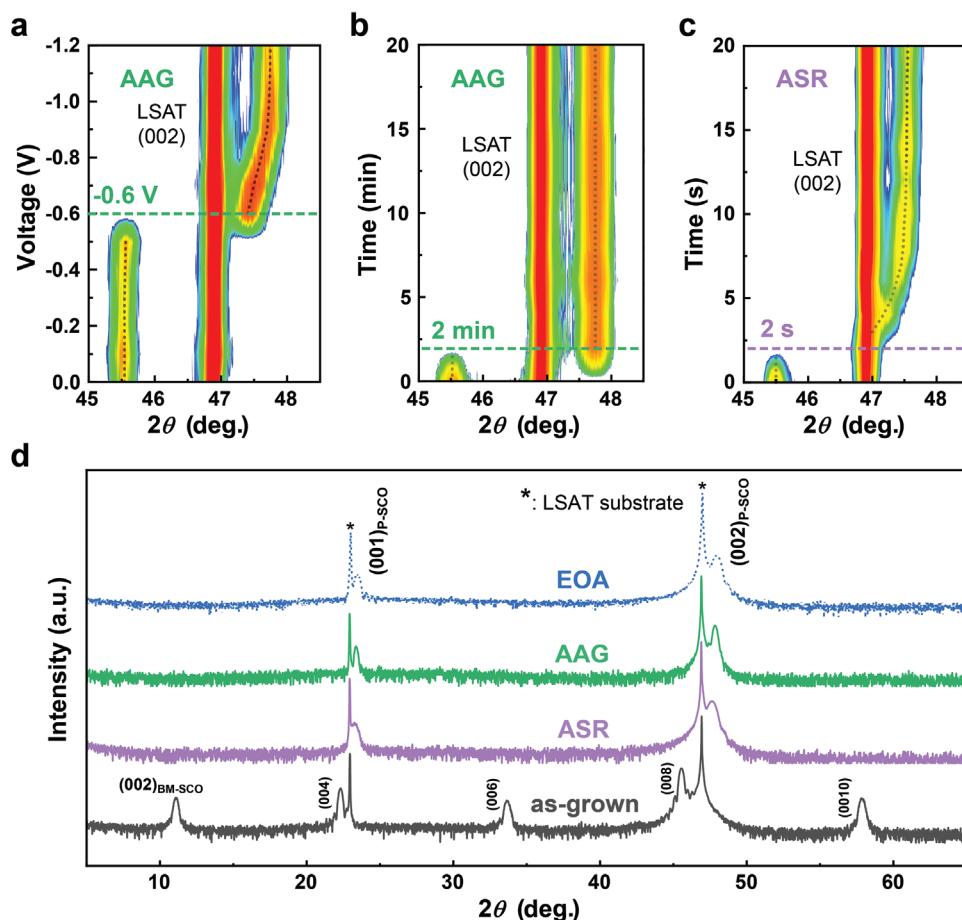
Figure 2. a) in situ voltage-dependent X-ray diffraction (XRD) studies of AAG-induced phase transition at various negative voltages. b) in situ time-dependent phase transition through the AAG method at −1 V. c) 2θ-ω scans of samples after different times of ASR. The experiments were carried out within HAc (36%). d) Comparison of large-range X-ray 2θ-ω scans for as-grown BM-SCO and P-SCO thin films obtained through different methods. The substrates employed are LSAT (001).

which are attributed to the alternating stacking of the oxygen octahedra and tetrahedra. While for all the other samples obtained from AAG, ASR, and EOA methods, we obtained very similar XRD results, with the completely disappeared superlattice peaks as well as right-shift of thin film peaks, providing strong evidence for the structural transition from BM-SCO to P-SCO. Moreover, the reciprocal space mapping and rocking curve measurements further confirmed the excellent crystalline quality of these P-SCO thin films obtained from both AAG and ASR methods (Figure S1, Supporting Information).

A detailed analysis of the XRD data (Figure 2d) reveals that these P-SCO samples show slightly different diffraction angles, indicating distinct c-lattice constant due to their varied oxygen contents, which is widely observed for P-SCO with an oxygen vacancy-induced lattice expansion.[36] To assess the physical properties of these P-SCO samples obtained from AAG and ASR methods, we performed both magnetic and electrical characterization. Distinct from the antiferromagnetic BM-SCO with zero magnetization, both P-SCO thin films show well-defined hysteresis loops, suggesting the development of a ferromagnetic state through the phase transition (**Figure 3**a). Notably, the sample obtained from the ASR method shows a slightly smaller

saturated magnetization as compared with the one obtained from AAG method. Such difference can be further resolved from the temperature-dependent measurements (Figure 3b), in which the transition temperatures are 200 K and 240 K for the ASR and AAG samples, respectively. Both these values are smaller than the previous results obtained from the ozone-annealed P-SCO and $SrCoO_3$ single crystal.[37] As the robust ferromagnetic state is strongly correlated to the double-exchange coupling among the high valent Co ions,[38,39] we attribute this slightly reduced magnetism to the presence of oxygen vacancies within the obtained P-SCO samples,[40,41] with more vacancies formed in the ASR sample as compared with the AAG and EOA samples. Such difference is consistent with the structural difference, in which the sample with more oxygen vacancy demonstrates a larger lattice expansion.[42]

To investigate the electrical properties of both P-SCO thin films, we carried out the temperature-dependent resistivity measurements as shown in Figure 3c. These two samples show a significantly reduced resistivity compared with the BM-SCO film, which is more than three orders of magnitude at room temperature. These results again indicate that both methods transform the insulating BM-SCO into conducting P-SCO.
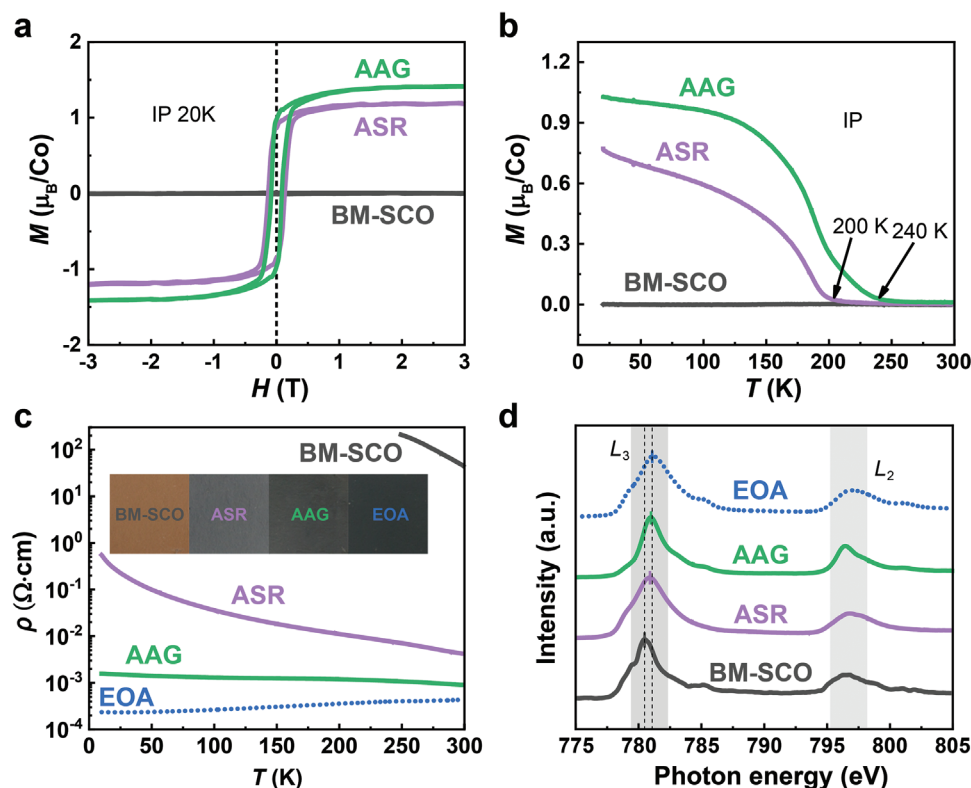
Figure 3. a) Magnetic hysteresis loops of BM-SCO and formed P-SCO thin films. The measurements were carried out at 20 K with the magnetic field applied within the film plane. b) In-plane temperature-dependent magnetization for different samples. The measurements were carried out with a magnetic field of 0.1 T after a field cooling from 300 K to 20 K at 2 T. c) Temperature-dependent electrical resistivity of pristine BM-SCO thin film and formed P-SCO thin films through AAG and ASR methods. The ex-situ ozone annealing (EOA) sample is also shown for comparison. d) Soft X-ray absorption spectra (sXAS) at Co L-edges for as-grown BM-SCO and formed P-SCO thin films through different methods.

Specifically, the metallic property of the AAG sample is very close to that of the EOA sample, with a negligible temperature dependence, while the ASR sample shows a semiconducting behavior in which the resistivity increases with the decrease of the temperature. These changes can also be resolved from the optical measurements. As shown in the inset of Figure 3c, all P-SCO samples show blackish colors, while the BM-SCO is brownish, suggesting the different electronic structures. While among the P-SCO samples, the different contrasts should be attributed to the distinct metallicity, in which the Drude feature is strongly suppressed with a spectra weight transferred to higher photon energy in the less conducting P-SCO samples.[31]

We note that the previous study reveals an insulator-to-metal transition occurs around the oxygen vacancy concentration range of $\delta \approx 0.1$,[43] and therefore we speculate that the oxygen content within our P-SCO samples should be within this range. To provide direct insights into the electronic states, we performed valence-state-sensitive soft X-ray absorption spectroscopy (sXAS) at the Co L-edges. As shown in Figure 3d, we observe distinct spectra for all P-SCO samples compared to the reference BM-SCO samples, indicating the high valence state in Co ions through the phase transition.[44] Notably, there is a slight but detectable red-shift of sXAS peak positions (at both L_3 and L_2) for the ASR samples as compared with both the AAG and EOA samples, which should be attributed to

the different oxygen stoichiometries among these P-SCO samples.[45]

Thermostability experiments provided further evidence of distinct oxygen stoichiometry among these samples (Figure S2, Supporting Information). Figure S2d (Supporting Information) shows a summary of the transition temperatures from P-SCO to BM-SCO upon heating within an argon gas environment. Specifically, both the EOA and AAG samples show a similar critical temperature of ≈ 230–240 °C, which is close to the previously reported value of 210 °C obtained from thermal annealing.[16] Nevertheless, the ASR sample shows a dramatically reduced critical temperature of 170 °C. With these results, we could deduce that the phase transition temperature is inversely proportional to the oxygen vacancy content within the P-SCO sample (as shown in Figure S2d, Supporting Information). Another feature closely related to thermostability and oxygen stoichiometry is the morphology of the P-SCO thin films. Compared with the as-grown BM-SCO, which possesses an atomic smooth morphology (Figure S3a, Supporting Information), the P-SCO samples show an interesting correlation with the methods employed. Specifically, the sample obtained from EOA reaction shows a negligible change in the sample morphology and maintains nicely the atomic smooth surface (Figure S3b, Supporting Information). While for the sample obtained from AAG method, some small particles can be clearly visualized

from the sample surface (Figure S3c, Supporting Information), which might be related to the electrochemical corrosion. Finally, for the sample obtained from ASR method, the sample shows a ravine-like feature (Figure S3d, Supporting Information), which could be attributed to the strong chemical reactions.

We note that the AAG method shows a much-enhanced phase transition rate as compared with the ILG method, which points to distinct underlying mechanisms for these topotactic phase transitions. We first carried out a series of controlled experiments to clarify the role of hydroxyl ions during the AAG method. We note that in the conventional ILG-induced oxidation measurements, it is revealed that the residual water content (≈100 ppm) within the ILG is essential for phase transition as it provides the source of both oxygen and hydrogen ions through the water electrolysis process. Therefore, the critical gating voltage (≈1.5 V)[12] is determined by the water electrolysis process. While, within the aqueous alkali of 0.1 m KOH solution, the presence of hydroxyl ions can turn into the hydroxyl radical and then molecular oxygen, the most reactive species of oxygen, through the electrochemical reactions. As shown in Figure S4a (Supporting Information), with a gating voltage of −1 V and deionized water as an electrolyte, no phase transition can be triggered with a gating duration of 10 min. However, by slightly increasing the concentration of KOH to 0.001 m, the structural transition can be readily triggered. Notably, the transition process becomes robust for even stronger alkali solutions (e.g., 0.1 m KOH). We propose the following electrochemical pathway for the topotactic oxidation process:

$$4SrCoO_{2.5} + 2OH^- \rightarrow 4SrCoO_3 + 2H_2O + 2e^- \tag{1}$$
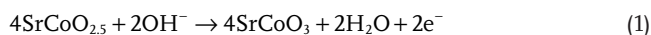
During this reaction, the abundant hydroxyl ions (OH⁻) within the KOH solution, as compared with that in the ionic liquid, promote the reaction rate, leading to reduced critical voltage and enhanced oxidation speed.

Since the acid solution is widely employed as a reducing agent, leading to the reduction of complex oxides, it is intriguing to discover the transition from BM-SCO to P-SCO in this study. To clarify the underlying mechanism, we first carried out a series of controlled experiments to understand the relationship between the concentration of proton (1<pH<7) and the phase transition. We found that for pH values >5, the phase transition is hardly observed, while for the solutions with lower (≤4) pH values, the phase transition occurs within 15 s (Figure S4b, Supporting Information). Interestingly, the reaction can occur in all tested acidic solutions (HAc, HCl, H₂SO₄, and even carbonated drinks) with enough proton concertation (pH value), regardless of the anions (Figure S4c, Supporting Information). Since the protons are very reductive, they would not trigger the oxidizing reaction alone. Then one might speculate that the oxidizing phase transition occurs with the assistance of the protons through a possible chemical pathway as:

$$4SrCoO_{2.5} + O_2 \xrightarrow{H^+} 4SrCoO_3 \tag{2}$$

In this process, the proton acts as the catalyst, which may reduce the oxygen adsorption and activation energies during the oxygen reduction reaction(ORR).[46] In this pathway, the

source of oxygen should be attributed to the dissolved oxygen molecules within the solution. To verify this scenario, we carried out a controlled experiment to trace the oxygen evolution with isotope oxygen as a tracer. We first introduced a large amount of ¹⁸O₂ molecules within both H₂SO₄ (0.02 m) and HAc (36%) solutions by inletting the gas flow (50 sccm for 3 min) within the solution. Then the BM-SCO sample was treated with this prepared acid solution, and a P-SCO sample was obtained. Finally, we carried out secondary-ion mass spectrometry (SIMS) measurements to probe the ¹⁸O contents within the sample. However, a negligible amount of ¹⁸O was determined (**Figure 4**a; Figure S5, Supporting Information), which can then safely exclude the participation of O₂ molecules during this phase transition.

Therefore, this controlled study further single out the protons as the dominating parameter for the observed phase transition. Accordingly, we proposed acid dissolution as a possible pathway. This hypothesis is supported by the experimental evidence that the thickness of ASR-induced P-SCO is significantly reduced compared with the initial BM-SCO sample (Figure 4b), indicating the dissolution of the thin film during the transition. In strong contrast, the P-SCO (with the Co octahedra, Co_{oct}) is more stable against the acid solution, with the crystalline structure preserved for a time duration of ≈1 min (Figure S4d, Supporting Information). While for longer soaking time (e. g., 5 min), the XRD peak for P-SCO totally disappears, which indicates that the whole sample is dissolved within the solution. This result demonstrates that the resistance of Co_{tet} (Co tetrahedra) and Co_{oct} to the acid are extremely different, and the Co_{tet} is considered as an active site for acid dissolution. Given that the only form of Co ions in acid solution is Co^{2+},[47] we propose a charge disproportionation process as summarized below:

$$2SrCoO_{2.5} + 4H^+ \rightarrow SrCoO_3 + Sr^{2+} + Co^{2+} + 2H_2O \tag{3}$$
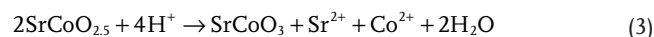
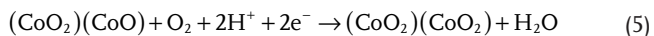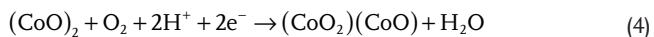For this redox reaction, the BM-SCO reacts with the protons, and half of the Co ions are reduced to dissolvable Co^{2+}, while the other half is oxidized into Co^{4+} in the form of P-SCO. To verify this mechanism, we measured the elemental concentration within the solution using inductively coupled plasma-Mass Spectrometry (ICP-MS). We chose 4 mL sulfuric acid (c[H⁺] = 0.01 mol L⁻¹) as acid solution and then soaked the BM-SCO film (with a thickness of 26 nm and an area of 25 mm²) within the solution for 15 s. The subsequent ICP-MS measurements reveal a substantial amount of Co ions (2715 nmol L⁻¹) within the acid solution after the reaction, which is consistent with the theoretical value of 2269 nmol L⁻¹ calculated based on our proton-assist ionic disproportionation model.

Additionally, density functional theory calculations (see Experimental Section) were performed to provide further insights into this exotic transition. Theoretical results reveal that the acid-catalytically-assisted oxidation process (Equation 2) is an endothermic reaction, indicating that this reaction cannot occur spontaneously. In contrast, the surface oxidation and acid dissolution processes are exothermic and could occur spontaneously within the acid solution. Specifically, the spontaneous oxidation reaction of the Co—O plane in the surface tetrahedral (Co_{tet}) layer (as illustrated in Figure S6a,b, Supporting
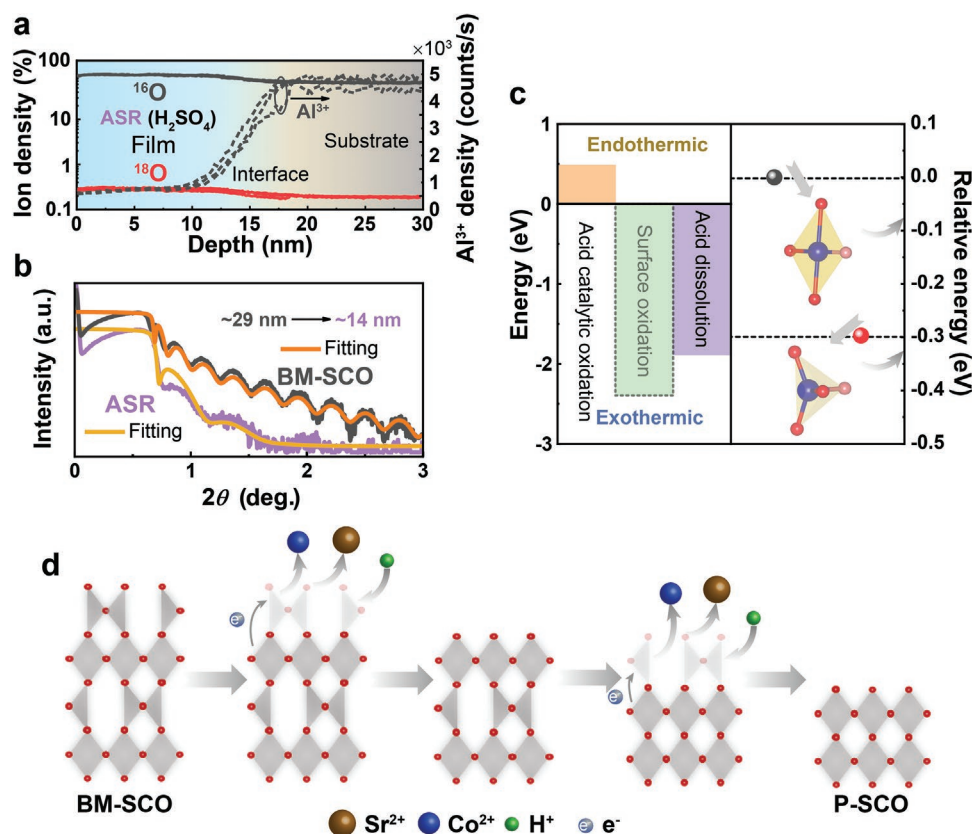
Figure 4. a) Depth profiles of ^{16}O and isotope ^{18}O within P-SCO sample obtained with the ASR method. Al^{3+} signal was employed as a marker for the interface position. b) X-ray reflectometry (XRR) measurements and the corresponding fittings for as-grown SCO thin film and its counterpart P-SCO thin film obtained with ASR. c) Comparison of energy evolution for various possible processes during ASR method and the relative oxygen vacancy formation energies at Co_{tet} and Co_{oct}. These results were obtained from density functional theory calculations. d) Schematic illustration of reaction steps in ASR through the acid-induced dissolution process.

Information) requires hydrogen ions, electrons, and oxygen vacancies. Thus, the oxidation of the surface Co−O plane could be described in the following steps (Equation 4,5):

$$(CoO)_2 + O_2 + 2H^+ + 2e^- \rightarrow (CoO_2)(CoO) + H_2O \quad (4)$$

$$(CoO_2)(CoO) + O_2 + 2H^+ + 2e^- \rightarrow (CoO_2)(CoO_2) + H_2O \quad (5)$$

Although this process is exothermic, the lack of extra electrons in this electrically neutral system puts an insurmountable challenge for this proposal, making the surface oxidation process unlikely. Indeed, it is also against our experimental evidence of the isotope oxygen evolution (Figure 4a).

Nevertheless, we found that the acid dissolution reaction (Equation 3) was also exothermic (Figure 4c). Noting that the BM-SCO sample possesses both Co_{tet} and Co_{oct} polyhedral units, we further explored their relation to the P-SCO formation by evaluating the corresponding oxygen vacancy formation energy (Figure S7, Supporting Information). As summarized in the right panel of Figure 4c, there is a clear different oxygen vacancy formation energy between Co_{oct} and Co_{tet}, with the Co_{tet} having the lower oxygen vacancy formation energy by 0.3 eV. In other words, when in contact with the protons in the

acid solution, the Co-O bonds within Co_{tet} tend to break due to the formation of additional oxygen vacancies. Notably, the obtained Co^{2+} is dissolvable within the water.

To obtain a clear picture of the acid-assisted dissolution process, we prepared a thicker (80 nm) BM-SCO sample and monitored its ASR-induced phase transition at short time intervals. The XRD results show the emergence of a mixed structure with both BM-SCO and P-SCO phases during the reaction (Figure S8a, Supporting Information), which is in strong contrast with the result obtained from thinner sample (30 nm) as shown in Figure 2c. Since a larger sample (10 mm × 10 mm, in Figure S8b, Supporting Information) shows a similar result to the smaller one (4 mm × 4 mm), we attributed the observed XRD results in Figure S8a (Supporting Information) to phase separation along the film normal. With this, a surface-to-bulk reaction model can be constructed, as shown in Figure S8c (Supporting Information), and the whole reaction process during ASR is illustrated in Figure 4d. Over this process, the acid solution first dissolves the surface Co_{tet} layer. Afterward, the oxygen vacancies migrate from the underneath Co_{tet} layer (with energy barriers of 0.81 eV and 1.21 eV for the two steps as shown in Figure S6b,c, Supporting Information) to form another surface Co_{tet} layer to continue the reaction. Consequently, such oxygen vacancy exchange leads to the

formation of P-SCO underneath. Due to a relatively smaller oxygen vacancy migration barrier with BM-SCO, we expect that the oxygen vacancy exchange process will be extended through the samples and eventually leads to the complete phase transition from BM-SCO and P-SCO. Due to such a strong chemical reaction, the sample morphology is strongly deformed into a ravine-like feature (Figure S3d, Supporting Information), which is starkly in contrast with the atomic smooth surface of the starting BM-SCO sample (Figure S3a, Supporting Information). Furthermore, it is naturally expected that the sample thickness will be dramatically suppressed along this process (as illustrated in Figure S8c, Supporting Information).

3. Conclusion

In summary, we have successfully demonstrated two strategies, AAG and ASR, to achieve the phase transition from BM-SCO to P-SCO at a considerable reaction rate. The magnetic and electrical properties in the obtained P-SCO thin films were systematically investigated, and their close correlations with the valence state of Co ions and oxygen vacancy concentration were revealed. Moreover, the underlying mechanisms of these newly demonstrated methods were carefully analyzed. Our study provides a deep understanding of the chemical activity of the brownmillerite structure and opens new pathways to manipulate the oxygen ionic evolution in complex oxide to design novel physical properties and improved functionalities.

Supporting Information

Supporting Information is available from the Wiley Online Library or from the author.

Conflict of Interest

The authors declare no conflict of interest.

Data Availability Statement

The data that support the findings of this study are available from the corresponding author upon reasonable request.

[1] R. E. Somekh, M. G. Blamire, Z. H. Barber, K. Butler, J. H. James, G. W. Morris, E. J. Tomlinson, A. P. Schwarzenberger, W. M. Stobbs, J. E. Evetts, *Nature* **1987**, *326*, 857.

[2] H. Kuwahara, Y. Tomioka, Y. Moritomo, A. Asamitsu, M. Kasai, R. Kumai, Y. Tokura, *Science* **1996**, *272*, 80.

[3] W. Eerenstein, N. D. Mathur, J. F. Scott, *Nature* **2006**, *442*, 759.

[4] J. Suntivich, K. J. May, H. A. Gasteiger, J. B. Goodenough, Y. Shao-Horn, *Science* **2011**, *334*, 1383.

[5] Y. Zhou, X. Guan, H. Zhou, K. Ramadoss, S. Adam, H. Liu, S. Lee, J. Shi, M. Tsuchiya, D. D. Fong, S. Ramanathan, *Nature* **2016**, *534*, 231.

[6] X. Mou, J. Tang, Y. Lyu, Q. Zhang, S. Yang, F. Xu, W. Liu, M. Xu, Y. Zhou, W. Sun, Y. Zhong, B. Gao, P. Yu, H. Qian, H. Wu, *Sci. Adv.* **2021**, *7*, eabh0648.

[7] H. Y. Huang, C. Ge, Q. H. Zhang, C. X. Liu, J. Y. Du, J. K. Li, C. Wang, L. Gu, G. Z. Yang, K. J. Jin, *Adv. Funct. Mater.* **2019**, *29*, 1902702.

[8] T. Katase, Y. Suzuki, H. Ohta, *J. Appl. Phys.* **2017**, *122*, 135303.

[9] C. Ge, C.-x. Liu, Q.-l. Zhou, Q.-h. Zhang, J.-y. Du, J.-k. Li, C. Wang, L. Gu, G.-z. Yang, K.-j. Jin, *Adv. Mater.* **2019**, *31*, 1900379.

[10] A. Muñoz, C. de la Calle, J. A. Alonso, P. M. Botta, V. Pardo, D. Baldomir, J. Rivas, *Phys. Rev. B* **2008**, *78*, 054404.

[11] J. Kuneš, V. Křápek, N. Parragh, G. Sangiovanni, A. Toschi, A. V. Kozhevnikov, *Phys. Rev. Lett.* **2012**, *109*, 117206.

[12] N. Lu, P. Zhang, Q. Zhang, R. Qiao, Q. He, H.-B. Li, Y. Wang, J. Guo, D. Zhang, Z. Duan, Z. Li, M. Wang, S. Yang, M. Yan, E. Arenholz, S. Zhou, W. Yang, L. Gu, C.-W. Nan, J. Wu, Y. Tokura, P. Yu, *Nature* **2017**, *546*, 124.

[13] Y. Gu, K. Xu, C. Song, X. Zhong, H. Zhang, H. Mao, M. S. Saleem, J. Sun, W. Liu, Z. Zhang, F. Pan, J. Zhu, *ACS Appl. Mater. Interfaces* **2019**, *11*, 19584.

[14] H.-Y. Lo, C.-Y. Yang, G.-M. Huang, C.-Y. Huang, J.-Y. Chen, C.-W. Huang, Y.-H. Chu, W.-W. Wu, *Nano Energy* **2020**, *72*, 104683.

[15] O. T. Tambunan, K. J. Parwanta, S. K. Acharya, B. W. Lee, C. U. Jung, Y. S. Kim, B. H. Park, H. Jeong, J.-Y. Park, M. R. Cho, Y. D. Park, W. S. Choi, D.-W. Kim, H. Jin, S. Lee, S. J. Song, S.-J. Kang, M. Kim, C. S. Hwang, *Appl. Phys. Lett.* **2014**, *105*, 063507.

[16] H. Jeen, W. S. Choi, M. D. Biegalski, C. M. Folkman, I. C. Tung, D. D. Fong, J. W. Freeland, D. Shin, H. Ohta, M. F. Chisholm, H. N. Lee, *Nat. Mater.* **2013**, *12*, 1057.

[17] P. Agrawal, *Phys. Rev. B* **2016**, *94*, 104101.

[18] J. R. Petrie, C. Mitra, H. Jeen, W. S. Choi, T. L. Meyer, F. A. Reboredo, J. W. Freeland, G. Eres, H. N. Lee, *Adv. Funct. Mater.* **2016**, *26*, 1564.

[19] D. Zhang, H. Ishizuka, N. Lu, Y. Wang, N. Nagaosa, P. Yu, Q.-K. Xue, *Phys. Rev. B* **2018**, *97*, 184433.

[20] D. Wang, L. Meng, L. Wei, P. Shi, Y. Chen, S. Yan, Y. Tian, G. Liu, L. Mei, *J. Magn. Magn. Mater.* **2020**, *496*, 165926.

[21] Q. Yang, H. J. Cho, H. Jeen, H. Ohta, *Adv. Mater. Interfaces* **2019**, *6*, 1901260.

[22] Q. Lu, S. Huberman, H. Zhang, Q. Song, J. Wang, G. Vardar, A. Hunt, I. Waluyo, G. Chen, B. Yildiz, *Nat. Mater.* **2020**, *19*, 655.

[23] Q. Yang, J. Lee, H. Jeen, H. J. Cho, H. Ohta, *ACS Appl. Electron. Mater.* **2021**, *3*, 3296.

[24] S. Hu, W. Han, S. Hu, J. Seidel, J. Wang, R. Wu, J. Wang, J. Zhao, Z. Xu, M. Ye, L. Chen, *Chem. Mater.* **2019**, *31*, 6117.

[25] Q. Lu, B. Yildiz, *Nano Lett.* **2016**, *16*, 1186.

[26] T. Katase, Y. Suzuki, H. Ohta, *Adv. Electron. Mater.* **2016**, *2*, 1600044.

[27] H. Jeen, W. S. Choi, J. W. Freeland, H. Ohta, C. U. Jung, H. N. Lee, *Adv. Mater.* **2013**, *25*, 3651.

[28] A. Nemudry, P. Rudolf, R. Schöllhorn, *Chem. Mater.* **1996**, *8*, 2232.

[29] L. Hao, Z. F. Zhang, X. Xie, H. R. Wang, Q. X. Yu, H. Zhu, *J. Cryst. Growth* **2015**, *427*, 36.

[30] D. Zhang, Y. Wang, N. Lu, X. Sui, Y. Xu, P. Yu, Q.-K. Xue, *Phys. Rev. B* **2019**, *100*, 060403.

[31] Y. Wang, Q. He, W. Ming, M.-H. Du, N. Lu, C. Cafolla, J. Fujioka, Q. Zhang, D. Zhang, S. Shen, Y. Lyu, A. T. N'Diaye, E. Arenholz, L. Gu, C. Nan, Y. Tokura, S. Okamoto, P. Yu, *Phys. Rev. X* **2020**, *10*, 021030.

[32] S. Hu, Z. Yue, J. S. Lim, S. J. Callori, J. Bertinshaw, A. Ikeda-Ohno, T. Ohkochi, C.-H. Yang, X. Wang, C. Ulrich, J. Seidel, *Adv. Mater. Interfaces* **2015**, *2*, 1500012.

[33] S. Hu, J. Seidel, *Nanotechnology* **2016**, *27*, 325301.

[34] S. Hu, Y. Wang, C. Cazorla, J. Seidel, *Chem. Mater.* **2017**, *29*, 708.

[35] H. Peng, N. Lu, S. Yang, Y. Lyu, Z. Liu, Y. Bu, S. Shen, M. Li, Z. Li, L. Gao, *Adv. Funct. Mater.* **2022**, *32*, 2111907.

[36] H. Jeen, H. N. Lee, *AIP Adv.* **2015**, *5*, 127123.

[37] Y. Long, Y. Kaneko, S. Ishiwata, Y. Taguchi, Y. Tokura, *J Phys Condens Matter* **2011**, *23*, 245601.

[38] R. H. Potze, G. A. Sawatzky, M. Abbate, *Phys. Rev. B* **1995**, *51*, 11501.

[39] C. Zener, *Phys. Rev.* **1951**, *82*, 403.

[40] C. K. Xie, Y. F. Nie, B. O. Wells, J. I. Budnick, W. A. Hines, B. Dabrowski, *Appl. Phys. Lett.* **2011**, *99*, 052503.

[41] F. J. Rueckert, Y. F. Nie, C. Abughayada, S. A. Sabok-Sayr, H. E. Mohottala, J. I. Budnick, W. A. Hines, B. Dabrowski, B. O. Wells, *Appl. Phys. Lett.* **2013**, *102*, 152402.

[42] H. Taguchi, M. Shimada, M. Koizumi, *J. Solid State Chem.* **1979**, *29*, 221.

[43] S. Balamurugan, K. Yamaura, A. B. Karki, D. P. Young, M. Arai, E. Takayama-Muromachi, *Phys. Rev. B* **2006**, *74*, 172406.

[44] S. Chowdhury, A. Jana, A. Kumar Mandal, R. J. Choudhary, D. M. Phase, *ACS Appl. Electron. Mater.* **2021**, *3*, 3060.

[45] L. Karvonen, M. Valkeapää, R.-S. Liu, J.-M. Chen, H. Yamauchi, M. Karppinen, *Chem. Mater.* **2010**, *22*, 70.

[46] V. Jovancicevic, J. O. M. Bockris, *J. Electrochem. Soc.* **1986**, *133*, 1797.

[47] S. G. Bratsch, *J. Phys. Chem. Ref. Data* **1989**, *18*, 1.